Defect Motifs for Constant Mean Curvature Surfaces

Halim Kusumaatmaja and David J. Wales

University Chemical Laboratories, University of Cambridge, Lensfield Road, Cambridge CB2 1EW, United Kingdom

(Received 22 June 2012; revised manuscript received 13 December 2012; published 15 April 2013)

The energy landscapes of electrostatically charged particles embedded on constant mean curvature surfaces are analyzed for a wide range of system size, curvature, and interaction potentials. The surfaces are taken to be rigid, and the basin-hopping method is used to locate the putative global minimum structures. The defect motifs favored by potential energy agree with experimental observations for colloidal systems: extended defects (scars and pleats) for weakly positive and negative Gaussian curvatures, and isolated defects for strongly negative Gaussian curvatures. Near the phase boundary between these regimes, the two motifs are in strong competition, as evidenced from the appearance of distinct funnels in the potential energy landscape. We also report a novel defect motif consisting of pentagon pairs.

DOI: 10.1103/PhysRevLett.110.165502 PACS numbers: 61.72.Bb, 02.60.Pn, 61.72.Lk, 64.70.pv

Introduction.—The distribution of electrostatically charged particles on curved surfaces [1] provides a testing ground for global optimization algorithms [2–7], as well as useful insights into a number of materials science and biological applications, including the packing of virus capsids [8,9], fullerene structures [10,11], colloidal crystals [12,13], and proteins on lipid membranes [14]. A key issue in understanding the resulting structures is the appearance of defects, which strongly influence the mechanical, electronic, and optical properties. Defect structures have even been exploited for the rational design of templated self-assembly; for example, polar defects have been used to create divalent metal nanoparticles [15].

Frustration is intrinsic to curved surfaces because of the competition between local order and long-range geometrical constraints, and defects appear to screen the resulting geometrical stresses, even for the ground state configuration. For example, while a hexagonal lattice is possible for a flat surface, this arrangement cannot occur on a sphere without introducing isolated fivefold disclinations (pentagons with positive topological charges), or composite structures with sevenfold disclinations (heptagons with negative topological charges) [2–7,12,16,17]. Generally, adjacent combinations of pentagons and heptagons may appear as topologically uncharged or charged lines of dislocations, corresponding to pleats (e.g., pentagon-heptagon topological dipoles) and scars (e.g., pentagon-heptagon-pentagon arrangements), respectively.

Isolated heptagons may also exist if the Gaussian curvature of the substrate is strongly negative, as was shown recently in studies of two-dimensional colloidal crystals on the surface of capillary bridges [18]. By systematically varying the shape and thus the curvature of the substrate, a sequence of transitions was observed from zero defects to isolated dislocations, pleats, scars, and isolated disclinations.

In the present contribution, we characterize the energy landscape of electrostatically charged particles embedded on constant mean curvature surfaces, modeling, in particular, the recent experimental setup by Irvine *et al.* for colloidal crystals [18,19]. Employing the basin-hopping algorithm [20–23], we identify likely global minimum configurations for a wide range of system sizes and surface curvatures, considering several different interaction potentials. Not only are we able to reproduce the experimental sequence of defect transitions, but we also identify a new defect motif corresponding to pentagon pairs, which may appear on surfaces with both positive and negative Gaussian curvatures. Furthermore, we show here for the first time the hierarchical nature of the potential energy landscape for these systems. Using disconnectivity graphs [24], we demonstrate the appearance of separate funnels in the landscape, corresponding to competing defect motifs favoring dislocations and disclinations. Our analysis also provides information on the rearrangement mechanisms between defect patterns, as well as insight into likely thermodynamic signatures for structural transitions.

Methodology.—We consider N identical electrostatically charged particles embedded on the surface of catenoids (zero mean curvature) and unduloids (nonzero mean curvature) [25]. To represent the interactions of these colloids trapped on fluid interfaces [26], we have mainly considered Yukawa potentials of the form $V = \sum_{j>i}^{N} \frac{1}{r_{ij}} e^{-(r_{ij}/\lambda)}$, where r_{ij} is the Euclidean distance between particles i and j, and λ is the screening length. We choose $\lambda = 0.1$ so that the ratio between the screening length and the length of the capillary bridges is of the same order as that used in experiments [18,26].

We have also considered four other potentials: a Yukawa potential with $\lambda = 0.4$, Coulomb, Lennard-Jones, and a repulsive Lennard-Jones form. Qualitatively, the defect motifs are the same provided that the particle density per

unit area is sufficiently high, indicating that our defect analysis should have wide-ranging applicability to curved surfaces. This regime corresponds to $N > 200$. If the number of electrostatically charged particles is smaller, they tend to populate the boundaries when Coulomb or other similarly long-range potentials are used; for the Lennard-Jones potential, we observe patches of a hexagonal lattice separated by large spaces. We therefore focus on $200 < N < 600$ in the present work.

Any point on the surface of an unduloid or a catenoid can be parametrized using two variables u and v [27]. For catenoids, the mapping to Cartesian coordinates takes the following form: $(x, y, z) = (c\cosh(v/c)\cos(u), c\cosh(v/c)\sin(u), v)$, where $0 \le u < 2\pi$, $-z_m \le v \le z_m$, and c is a free parameter corresponding to the waist of the catenoid in the $z = 0$ plane. The corresponding transformation is more elaborate for unduloids $(x, y, z) = ((m\sin\mu v + n)^{1/2}\cos(u), (m\sin\mu v + n)^{1/2}\sin(u), aF(\mu v/2 - \pi/4, k) + cE(\mu v/2 - \pi/4, k))$, with $\mu = 2/(a + c)$, $k^2 = (c^2 - a^2)/c^2$, $m = (c^2 - a^2)/2$, and $n = (c^2 + a^2)/2$. $F(\phi, k)$ and $E(\phi, k)$ are elliptic integrals of the first and second kinds. We tune the shape of the unduloids by varying the parameters a, c, and the range of values for v [27]. For a neck shape unduloid [e.g., Figs. 1(a)–1(c)], v is centred around $v_c = 3\pi/2\mu$, while for a barrel shape unduloid, $v_c = \pi/2\mu$. The maximum and minimum values of v are chosen so that $-z_m \le z \le z_m$.

To characterize the most favorable geometries we employ basin-hopping global optimization [20–23]. In this method, random geometrical perturbations are followed by energy minimization, and moves are accepted or rejected based upon the energy differences between local minima. The minimization procedure transforms the energy landscape of the system into the set of catchment basins for the local minima, and makes the basin-hopping method very effective for finding low-lying structures. Further details are provided in the Supplemental Material [28].

We have also constructed databases of connected minima for selected systems, starting from the low-lying structures found in the basin-hopping runs. We employed doubly-nudged elastic band transition state searches [29], where images corresponding to local maxima were tightly converged to transition states using a hybrid eigenvector-following [30,31]. This procedure provides a global survey of the potential energy landscape, which we then visualize using disconnectivity graphs [24]. We find that distinct structural arrangements of the particles result in separate funnels in the landscape. Moreover, the database of connected minima and transition states allows us to predict energy barriers and rearrangement mechanisms between defect rearrangements.

To visualize the defect structures, we use Voronoi constructions. Thus, pentagons, hexagons, and heptagons correspond to particles with five, six, and seven neighbors. All the results presented here were obtained using the GMIN, OPTIM, and PATHSAMPLE programs [32], which are available for use under the GNU public license.

Defect motifs on unduloids.—We first analyze the arrangement of electrostatically charged particles embedded on nonzero constant mean curvature surfaces (unduloids). The results for $N = 600$ identical particles are presented in Fig. 1. The unduloid parameters a and c were varied while keeping the height ($2z_m = 1.5$) and volume ($V = 2.65$) of the unduloids constant. Experimentally, these parameters correspond to capillary bridges for

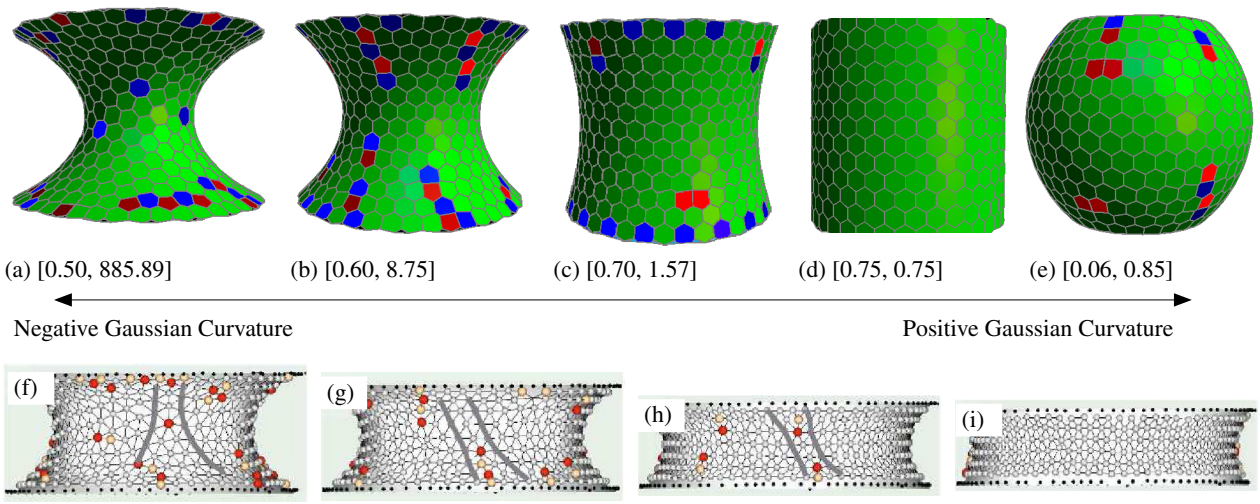

FIG. 1 (color online). Defect motifs for nonzero constant mean curvature surfaces. (a)–(e) The number of electrostatically charged particles is $N = 600$, and the curvature of the capillary bridges is varied while keeping the height and volume of the bridges constant. The corresponding values for the unduloid parameters $[a, c]$ are given in square brackets. (f)–(i) Comparisons to experimental results of Irvine *et al.* for colloidal crystals, reproduced from Ref. [18]. In the experiments, the curvature is tuned by stretching or compressing the liquid bridge, and the sequence of defect transitions observed is identical to our global optimization results.

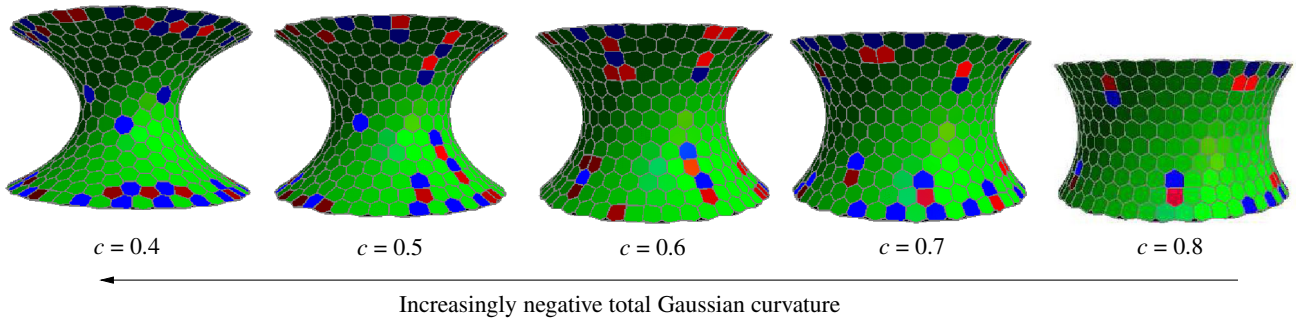

FIG. 2 (color online). Defect motifs on catenoid surfaces for $N = 600$, with variable waist radius c.

surfaces with different contact angles [33,34]. The defect motifs and sequence of transitions were found to be consistent as we varied the number of particles, and specific results for $N = 200$ are presented in the Supplemental Material [28].

Because of the finite number of particles, edge effects are an intrinsic feature and we find that the first two rows of Voronoi cells from the boundary consistently have more defects. As for the experimental results on colloidal crystals [18], we find a series of defect transitions, including isolated heptagons (Fig. 1). The Gaussian curvature is not constant on the surface of an unduloid, and it is most negative at the waist, where isolated heptagons are located [Fig. 1(a)]. Far from the waist and near the edge of the unduloid, we observe lines of dislocations.

For less negative total Gaussian curvatures [Figs. 1(b) and 1(c)], isolated heptagons disappear and dislocation lines prevail. The length of the dislocations is also found to correlate strongly with the curvature: the length is shorter when the curvature is less negative. For weakly negative Gaussian curvatures, the pentagon-heptagon dipole is a common motif, together with a pair of pentagons. The pentagon pair motif is surrounded by seven hexagons, as for an isolated heptagon, and to the best of our knowledge, this motif has not been reported before. Since isolated pentagons have a positive topological charge, it is somewhat surprising that double pentagons may exist in a bound state, and that they can be favorable for surfaces with a negative Gaussian curvature.

We observe no defects for cylinders [zero Gaussian curvature, Fig. 1(d)], as expected. Dislocation lines as well as pentagon pairs then reappear for the unduloid with a positive total Gaussian curvature [Fig. 1(e)]. The orientations of the dislocations and pentagon pairs are reversed for surfaces with positive and negative Gaussian curvatures. As predicted by continuum elastic theories [18,35], for negative curvatures, the 7-5 dislocation axis runs along the meridian, pointing in the direction of the boundary. For positive Gaussian curvatures, the dislocation axis points to the center of the unduloid instead. Similarly, the pentagon pairs point to the boundary for negative Gaussian curvatures, and to the center of the unduloids for positive Gaussian curvatures.

Defect motifs on catenoids.—We have also analyzed the defect structures for a family of catenoids (minimal surfaces) with varying values of the waist parameter c. We adjust the height parameter z_m so that the radius of the catenoid at z_m, $c\cosh(z_m/c) = 1$. This procedure results in less negative total Gaussian curvatures with an increasing waist radius c; see Fig. 2.

For a strongly negative Gaussian curvature (small c in Fig. 2), we always observe isolated heptagons at the waist of the catenoids, independent of N. We illustrate the disconnectivity graph [36] for $N = 600$ and $c = 0.40$ in Fig. 4(a). The potential energy landscape is clearly hierarchical in character. Interestingly, there are only two dominant defect configurations near the waist with a high degree of symmetry, which we label as α and β in the inset, each consisting of eight heptagons. The main variation in the structural arrangements of the ions comes from the dislocation lines near the edges (see the Supplemental Material for animations of the structures shown in Fig. 4 [28]). The energy barrier for interconverting waist configurations α and β is approximately $\Delta E_1 \sim 0.4$ (in reduced units) if the configuration near the edge of the catenoid is roughly preserved. On the other hand, the barrier for rearranging the particle distribution near the edges can be much higher, $\Delta E_2 \sim 2.2$ (reduced units), as indicated in Fig. 4(a). From the pathway we see that the high barrier is due to the global concerted rotation of several layers of ions near the edges of the catenoids.

For weakly negative Gaussian curvatures (large c in Fig. 2), we never find isolated heptagons, and only lines of dislocations and pentagon pairs exist. It is worth noting that these defect motifs have the same orientations as for unduloids with a negative Gaussian curvature, above. The energy landscape for this parameter regime is also simpler. In particular, we find that the number of possible local minima is considerably smaller.

The transition from defect patterns favoring disclinations to dislocations occurs at moderately negative Gaussian curvatures, $c \sim 0.55$, which we determine by constructing a defect phase diagram as a function of the number of electrostatically charged particles N and the catenoid waist radius c (Fig. 3). Our global optimization results further suggest that this transition is only weakly

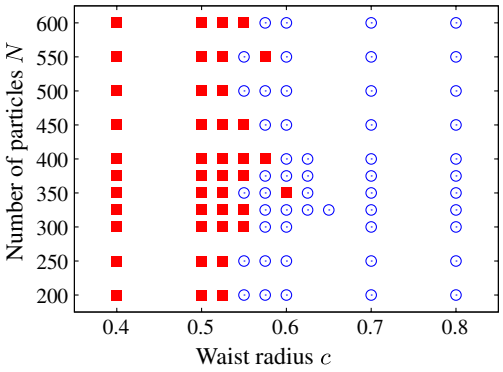

FIG. 3 (color online). Defect phase diagram as a function of the catenoid waist radius c and number of electrostatically charged particles N. Squares denote global minimum structures containing isolated heptagons, while circles correspond to structures without isolated heptagons.

dependant on the number of particles in this size range. The phase diagram for the repulsive Lennard-Jones potential is shown in the Supplemental Material [28], where we find similar behavior, except that the phase boundary is shifted to larger c. Our results for $N < 600$ are probably far from the continuum limit, where Bowick and Yao [35] predict that c will decrease monotonically with N. Additionally, the phase boundary found in Fig. 3 is neither smooth nor monotonic. We can explain this observation by analyzing the disconnectivity graph for $N = 600$ and $c = 0.575$. As shown in Fig. 4(b), there are two distinct funnels, one favoring dislocations and the other favoring disclinations. The energy difference between the lowest configurations in the two funnels is very small compared to the energy barrier ($\Delta E_3 \sim 0.7$ in reduced units) associated with interconverting the two defect motifs.

Discussion.—We have investigated the most favorable defect motifs for electrostatically charged particles embedded on zero and nonzero constant mean curvature surfaces. By varying the curvature of the embedding surface, we have characterized the detailed structures and energetics of a wide range of defect motifs, including dislocation lines and isolated disclinations, which are in excellent agreement with experiment and predictions from continuum elastic theories. The appearance of a new defect motif consisting of pentagon pairs is also predicted.

Taking the typical experimental values for electrostatic interactions between colloids embedded on interfaces, the energy scale for one simulation unit corresponds to between 10 and $100 k_B T$ (at room temperature). The energy barriers of interest, as shown in Fig. 4, are therefore quite large and the structures observed in experiments could be trapped in local minima. For experimentally relevant temperatures the favored defect motifs are primarily determined by the potential energy, which is consistent with the successful structure predictions that we have reported. We hope these results will stimulate future theoretical and experimental work. In particular, it will be interesting to modulate (reduce) the strength of interactions between the electrostatically charged colloids, so that the defect rearrangement mechanisms and thermodynamics of the system may be fully explored. Since the energy landscape is hierarchical, with different energy scales for interconverting the defect motifs, we expect the thermodynamics

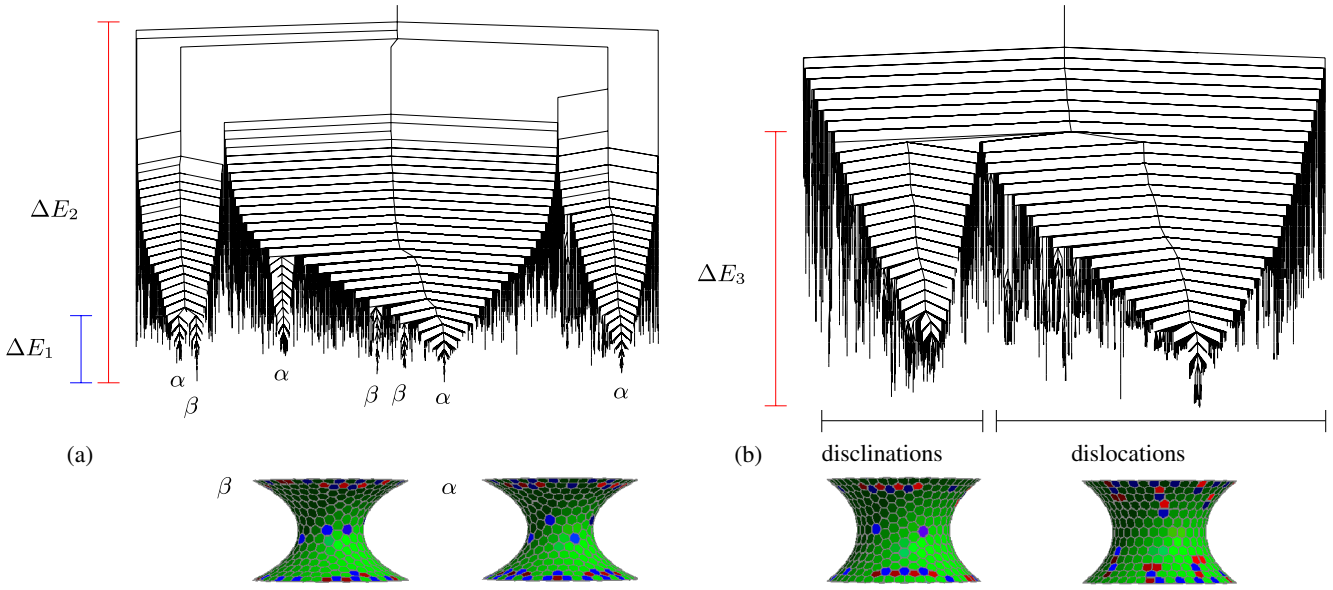

FIG. 4 (color online). Disconnectivity graphs for $N = 600$ electrostatically charged particles embedded on catenoids with waist radius (a) $c = 0.40$ and (b) $c = 0.575$. The structures in (a) and (b) show representative minima for the corresponding funnels in the potential energy landscape. We also indicate the typical energy barriers for interconverting different defect motifs. ΔE_1, ΔE_2, and ΔE_3 are, respectively, 0.4, 2.2, and 0.7 in reduced units.

of the system to be very rich. For example, we predict that there will be multiple signatures in the heat capacity corresponding to alternative defect morphologies [23]. Calculations of the thermodynamics, kinetic rates, and rearrangement pathways for these defect motif transitions are currently underway and will be presented elsewhere. The interplay between the arrangement of the electrostatically charged particles and possible deformation of the interface is still an open question, and allowing for flexible rather than rigid curved surfaces is another avenue for future research.

Analog models of the defect motifs presented here can be constructed using Polydron tiles [37], as illustrated in the Supplemental Material [28]. The Supplemental Material also contains animations of the defect morphologies shown in Figs. 1, 2, and 4, the tabulated numbers of positive and negative topological charges, and a detailed analysis of the net topological charges as a function of the integrated Gaussian curvature for several representative cases. The putative global minima found here will be made available online from the Cambridge Cluster Database [38].

This research was supported by EPSRC Programme Grant No. EP/I001352/1 and by the European Research Council Grant No. RG59508.

[1] J. J. Thomson, Philos. Mag. **7**, 237 (1904).
[2] L. T. Wille, Nature (London) **324**, 46 (1986).
[3] E. L. Altschuler, T. J. Williams, E. R. Ratner, F. Dowla, and F. Wooten, Phys. Rev. Lett. **72**, 2671 (1994).
[4] T. Erber and G. M. Hockney, Phys. Rev. Lett. **74**, 1482 (1995).
[5] T. Erber and G. M. Hockney, Adv. Chem. Phys. **98**, 495 (1997).
[6] D. J. Wales and S. Ulker, Phys. Rev. B **74**, 212101 (2006).
[7] D. J. Wales, H. McKay, and E. L. Altschuler, Phys. Rev. B **79**, 224115 (2009).
[8] D. L. D. Caspar and A. Klug, Cold Spring Harbor Symposia on Quantitative Biology (1933-) [Proceedings] **27**, 1 (1962).
[9] C. J. Marzec and L. A. Day, Biophys. J. **65**, 2559 (1993).
[10] H. W. Kroto, J. R. Heath, S. C. O'Brien, R. F. Curl, and R. E. Smalley, Nature (London) **318**, 162 (1985).
[11] A. Pérez-Garrido, Phys. Rev. B **62**, 6979 (2000).
[12] A. R. Bausch, M. J. Bowick, A. Cacciuto, A. D. Dinsmore, M. F. Hsu, D. R. Nelson, M. G. Nikolaides, A. Travesset, and D. A. Weitz, Science **299**, 1716 (2003).
[13] P. Lipowsky, M. J. Bowick, J. H. Meinke, D. R. Nelson, and A. R. Bausch, Nat. Mater. **4**, 407 (2005).
[14] R. N. Frese, J. C. Pàmies, J. D. Olsen, S. Bahatyrova, C. D. van der Weij-de Wit, T. J. Aartsma, C. Otto, C. N. Hunter, D. Frenkel, and R. van Grondelley, Biophys. J. **94**, 640 (2008).
[15] G. A. DeVries, M. Brunnbauer, Y. Hu, A. M. Jackson, B. Long, B. T. Neltner, O. Uzun, B. H. Wunsch, and F. Stellacci, Science **315**, 358 (2007).
[16] M. Bowick, A. Cacciuto, D. R. Nelson, and A. Travesset, Phys. Rev. Lett. **89**, 185502 (2002).
[17] M. J. Bowick and L. Giomi, Adv. Phys. **58**, 449 (2009).
[18] W. T. M. Irvine, V. Vitelli, and M. Chaikin, Nature (London) **468**, 947 (2010).
[19] W. T. M. Irvine, M. J. Bowick, and P. M. Chaikin, Nat. Mater. **11**, 948 (2012).
[20] Z. Li and H. A. Scheraga, Proc. Natl. Acad. Sci. U.S.A. **84**, 6611 (1987).
[21] D. J. Wales and J. P. K. Doye, J. Phys. Chem. A **101**, 5111 (1997).
[22] D. J. Wales and H. A. Scheraga, Science **285**, 1368 (1999).
[23] D. J. Wales, *Energy Landscapes* (Cambridge University Press, Cambridge, 2003).
[24] O. M. Becker and M. Karplus, J. Chem. Phys. **106**, 1495 (1997).
[25] C. Delauney, J. Math. Pures Appl., Sér. 1 **6**, 309 (1841).
[26] M. E. Leunissen, A. van Blaaderen, A. D. Hollingsworth, M. T. Sullivan, and P. M. Chaikin, Proc. Natl. Acad. Sci. U.S.A. **104**, 2585 (2007).
[27] M. Hadzhilazova, I. M. Mladenov, and J. Oprea, Archivum mathematicum : scripta Facultatis Scientiarum Naturalium Universitatis Purkynianae Brunensis **43**, 417 (2007).
[28] See Supplemental Material at http://link.aps.org/supplemental/10.1103/PhysRevLett.110.165502 for (i) detailed descriptions of the basin-hopping runs, (ii) highly symmetrical defect motifs for $N = 200$ charged particles embedded on unduloids, (iii) a defect phase diagram for a repulsive Lennard-Jones potential, (iv) animations of the defect morphologies shown in Figs. 1, 2, and 4, (v) tabulated numbers of positive and negative topological charges, (vi) detailed analysis of the net topological charges as a function of the integrated Gaussian curvature for several representative cases, (vii) analog models of the defect motifs constructed using Polydron tiles.
[29] S. A. Trygubenko and D. J. Wales, J. Chem. Phys. **120**, 2082 (2004).
[30] G. Henkelman, B. P. Uberuaga, and H. Jónsson, J. Chem. Phys. **113**, 9901 (2000).
[31] L. J. Munro and D. J. Wales, Phys. Rev. B **59**, 3969 (1999).
[32] http://www-wales.ch.cam.ac.uk/software.html.
[33] H. Kusumaatmaja and R. Lipowsky, Langmuir **26**, 18 734 (2010).
[34] E. J. D. Souza, M. Brinkmann, C. Mohrdieck, A. Crosby, and E. Arzt, Langmuir **24**, 10 161 (2008).
[35] M. J. Bowick and Z. Yao, Europhys. Lett. **93**, 36 001 (2011).
[36] In the disconnectivity graph, the vertical axis corresponds to the energy of the system. Each line ends with a local minimum. A node joins minima which can be interconverted without exceeding the energy of the node (thus providing information on the energy barriers between minima). For clarity, we discretize the energy in regular steps along the vertical axis.
[37] http://www.polydron.com/.
[38] http://www-wales.ch.cam.ac.uk/wales/CCD/ThomsonCMC/table.html.